

CONCERTO: Forward modelling of interferograms for calibration

A. Lundgren¹, A. Beelen¹, G. Lagache¹, F.-X. Désert², A. Fasano^{3,4}, J. Macias-Perez⁵, A. Monfardini⁸, P. Ade⁶, M. Aravena⁷, E. Barria⁸, A. Benoit⁸, M. Béthermin⁹, J. Bounmy⁵, O. Bourrion⁵, G. Bres⁸, C. De Breuck¹⁰, M. Calvo⁸, A. Catalano⁵, C. Dubois¹, C.A Durán^{10,11}, T. Fenouillet¹, J. Garcia¹, G. Garde⁸, J. Goupy⁸, C. Hoarau⁵, W. Hu¹², J.-C. Lambert¹, F. Levy-Bertrand⁸, J. Marpaud⁵, R. Parra¹³, G. Pisano⁶, N. Ponthieu², L. Prieur¹, D. Quinotoa¹⁴, S. Roni⁵, S. Roudier⁵, D. Tourres⁵, C. Tucker⁶, and M. Van Cuyck¹⁵

¹ Aix Marseille Univ, CNRS, CNES, LAM, Marseille, France, e-mail: andreas.lundgren@lam.fr

² Univ. Grenoble Alpes, CNRS, IPAG, 38400 Saint Martin d'Hères, France

³ Instituto de Astrofísica de Canarias, E-38205 La Laguna, Tenerife, Spain

⁴ Departamento de Astrofísica, Universidad de La Laguna (ULL), E-38206 La Laguna, Tenerife, Spain

⁵ Univ. Grenoble Alpes, CNRS, Grenoble INP, LPSC-IN2P3, 53, avenue des Martyrs, 38000 Grenoble, France

⁶ Astronomy Instrumentation Group, University of Cardiff, The Parade, CF24 3AA, United Kingdom

⁷ Instituto de Estudios Astrofísicos, Facultad de Ingeniería y Ciencias, Universidad Diego Portales, Av. Ejército 441, Santiago, Chile

⁸ Univ. Grenoble Alpes, CNRS, Grenoble INP, Institut Néel, 38000 Grenoble, France

⁹ Université de Strasbourg, CNRS, Observatoire astronomique de Strasbourg, UMR 7550, 67000 Strasbourg, France

¹⁰ European Southern Observatory, Karl Schwarzschild Straße 2, 85748 Garching, Germany

¹¹ Instituto de Radioastronomía Milimétrica (IRAM), Granada, Spain

¹² Department of Physics and Astronomy, University of the Western Cape, Robert Sobukhwe Road, Bellville, 7535, South Africa

¹³ ESO Vitacura, Alonso de Córdova 3107, Vitacura, Casilla 19001, Santiago de Chile, Chile

¹⁴ Observatorio Astronómico de Quito, Escuela Politécnica Nacional, Quito 170403, Ecuador

¹⁵ Department of Astronomy, University of Illinois, 1002 West Green Street, Urbana, IL 61801, USA

Received X X, XXXX; accepted X X, XXXX

ABSTRACT

Context. The CarbON [CII] line in post-reionisation and Reionisation epoch (CONCERTO) instrument was a low-resolution mapping Fourier-transform spectrometer based on lumped-element kinetic inductance detector (LEKID) technology that operated at 130–310 GHz. It was installed on the 12-meter APEX telescope in Chile in April 2021 and operated until December 2022. CONCERTO's main science goal is to constrain the [CII] line fluctuations at high redshift. To reach this goal, CONCERTO observed 1.4 deg² in the COSMOS field.

Aims. To ensure accurate calibration of the data, we developed a forward model capable of simulating the spectral response and the corresponding interferograms for each scan of observation in the COSMOS field. We present the modelling approach that enabled us to reproduce the expected instrument outputs under controlled input conditions and that provided a framework for the different calibration steps, including the absolute brightness calibration of the spectra.

Methods. We constructed a dedicated analysis pipeline to characterise the raw interferometric data (interferograms) obtained under a broad range of atmospheric conditions at APEX. Using the forward model, we measured the interferogram alignment with the optical path difference (zero path difference) and the relative response of each KID (flatfield). Together, these elements enabled us to characterise the instrument's spectral brightness calibration reliably.

Results. We demonstrate that the zero path difference systematically varies with elevation and across detectors, with variations that are consistent with small optical misalignments and elevation-dependent mechanical effects in the optical structure. The full measurement of these variations allowed us to construct a data base that is used to determine the zero path difference for each measured individual interferogram accurately. The flatfield shows systematic variations with detector position, but is extremely stable with time and atmospheric contribution. The accurate determination of the zero path differences and flatfields allowed us to construct spectral cubes that combine all detectors and all blocks of data. Finally, we present a novel method for calibrating the absolute brightness of these spectral cubes, which is agnostic to the exact knowledge of the bandpasses and directly applicable to extended emission.

Conclusions. Our analysis establishes a framework for precise calibration directly from on-sky data. This approach ensures a reliable performance for cosmological and astrophysical applications and can readily be adapted to future Martin-Puplett interferometer-based Fourier-transform spectrometers.

Key words. methods: data analysis; methods: observational; sub-millimetre: general; Instrumentation: miscellaneous

1. Introduction

Modern astrophysics increasingly relies on instruments of high complexity that are designed to address demanding scientific objectives with unprecedented accuracy. Meeting these objectives requires not only advances in hardware, but also a detailed un-

derstanding of the instrumental behaviour. Comprehensive modelling has thus become indispensable: it enables the prediction of performance, the identification and mitigation of systematic effects, and the validation of data analysis pipelines.

In the (sub-)millimetre, Fourier-transform spectrometer (FTS) mapping meets the requirements for wide-area cover-

age and low-resolution spectroscopy in astronomical observations. By recording interferograms generated from the superposition of two optical beams and applying Fourier analysis, FTS delivers spectral information with broad frequency coverage, modest spectral resolution (with $R \sim 100\text{--}500$), and full field of view (FoV) sampling in a single measurement. This combination has proven particularly valuable in studies of the cosmic microwave background (CMB), as exemplified by the Far-Infrared Absolute Spectrophotometer (FIRAS; [Mather et al. 1999](#)) and other space-borne instruments such as the Spectral and Photometric Imaging Receiver (SPIRE; [Griffin et al. 2010](#)). It has also been adopted as a baseline for several proposed above-the-atmosphere experiments, including the Primordial Inflation Explorer (PIXIE; [Kogut et al. 2025](#)) and the Balloon Interferometer for Spectral Observations of the primordial Universe (BISOU; [Maffei et al. 2024](#)). For ground-based observations, atmospheric fluctuations require the use of fast detectors, with kinetic inductance detectors (KIDs) representing a well-suited technology available in large-format arrays at millimetre wavelengths ([Catalano et al. 2020](#)). KIDs have already been deployed in photometric millimetre instruments such as the Néel IRAM KID Array (NIKA; [Monfardini et al. 2010](#)) and NIKA2 ([Adam et al. 2018](#)), which were both installed at the IRAM 30-m telescope at Pico Veleta, where NIKA2 remains in operation. A particularly well-suited implementation of FTS in this context is the Martin–Puplett interferometer (MPI; [Martin & Puplett 1970](#)), which has already been employed in experiments such as the KIDs Interferometric Spectral Surveyor (KISS; [Fasano et al. 2020](#)) and Osservatorio per il Lontano Infrarosso Montato su Pallone Orientabile (OLIMPO; [Masi et al. 2008](#)), and which constituted the core design of the CONCERTO spectrometer. The CONCERTO project ([Monfardini & Lagache 2021](#), [Concerto Collaboration et al. 2020](#)) was conceived as a pathfinder to demonstrate wide-field spectroscopic mapping of the millimetre sky using an MPI-based FTS coupled to KID arrays.

To maximise its scientific potential, CONCERTO relied on modelling approaches at different levels of detail, each designed to capture specific aspects of the instrument behaviour. We focused on a forward model of raw CONCERTO interferograms, designed to describe in detail how instrumental, optical, and environmental effects propagate into the measured interferometric signal. This interferogram-level modelling is a key ingredient for calibration, for the identification of systematic effects, and for the interpretation of the resulting spectra.

Higher-level end-to-end modelling aimed at reproducing global instrument performance and observational characteristics is beyond the scope of this work. We describe the forward modelling and characterisation of the raw interferograms measured by CONCERTO, together with the correction procedures required to reconstruct accurate spectra and derive their absolute calibration in astrophysical units.

The CONCERTO instrument was installed on the APEX telescope ([Güsten et al. 2006](#)) in April 2021. Commissioning runs were conducted shortly thereafter, and regular science operations took place between July 2021 and December 2022. The main scientific programme is a line-intensity mapping survey of the COSMOS field ([Scoville et al. 2007](#)), complemented by dedicated observations of the Sunyaev–Zeldovich effect in galaxy clusters, star-forming regions (including the Galactic centre), and evolved stars, all carried out during open time. For a comprehensive description of the observing campaign and operational procedures, we refer to [Hu et al. \(2024\)](#). The first scientific exploitation of CONCERTO data has recently been reported, with

observations of the Orion nebula revealing CO(2–1) and water emission lines alongside the continuum. These results show the instrument’s spectral capabilities (see [Désert et al. \(2025\)](#) for a detailed discussion).

The paper is organised as follows. Section 2 briefly presents the CONCERTO instrument. Section 3 describes the observations we used in our analysis. In Sect. 4 we provide a summary of the data reduction that is needed for our work. Section 5 develops the forward data model of CONCERTO raw interferograms, accounting for atmospheric emission, reference-source and stray-light contributions. In Section 6 we report on the measurements of the zero path difference and the instrumental response from interferogram timelines for each detector. In Sect. 7 we focus on an original method to derive the absolute brightness calibration of spectra. Finally, Sect. 8 summarises our conclusions and discusses prospects for future applications.

2. The instrument

The CONCERTO spectrometer employed an MPI configuration. This design was also used in its precursor, KISS ([Fasano et al. 2020](#), [Macías-Pérez et al. 2024](#)). The MPI combines two input sources and introduces an optical path difference (OPD) through the displacement of a rooftop mirror, producing an interferogram recorded at two complementary outputs, as illustrated in Fig. 1. By adjusting the stroke of the moving mirror, the OPD can be tuned, with longer strokes providing a higher spectral resolution.

For clarity, polarisers P1 and P2 are located at ambient pressure and temperature within the instrument enclosure, while polariser P3 is located inside the cryostat together with the LF and HF detector arrays, which operate under vacuum at cryogenic temperatures.

In the Martin–Puplett configuration, the interferometer intrinsically measures the differential signal between the sky-facing input and a reference input. In CONCERTO, two reference configurations are implemented:

- REFSKY: a defocused image of the ~ 18.6 arcmin instantaneous field of view, which optically subtracts the atmospheric common-mode spectrum and is well suited for compact sources, smaller than the FoV ([Concerto Collaboration et al. 2020](#); [Désert et al. 2025](#)).
- REFBB: a stabilised cold blackbody source, which serves as the reference for the present work (see Sect. 5.1.2 for details).

Since this paper exclusively addresses COSMOS data acquired in REFBB mode, our discussion focuses on this.

The transmission output corresponds to the low-frequency band (LF; 130–270 GHz), while the reflection output corresponds to the high-frequency band (HF; 195–310 GHz). A schematised view of the core of the instrument is presented in Fig. 1, highlighting key components such as the polariser P3, which splits the signal into the corresponding LF and HF focal planes.

The LF and HF arrays are large-format assemblies of lumped-element kinetic inductance detectors (LEKIDs), superconducting resonators operated at cryogenic temperatures. A central advantage of LEKIDs in Fourier transform spectroscopy is their ability to linearly record the large signal variations expected for interferograms of atmospheric emission. In these detectors, incident radiation modifies the kinetic inductance of the superconducting film, leading to a shift in the resonance frequency of each KID, which is monitored by the readout electronics. In addition, the intrinsic fast time response of LEKIDs

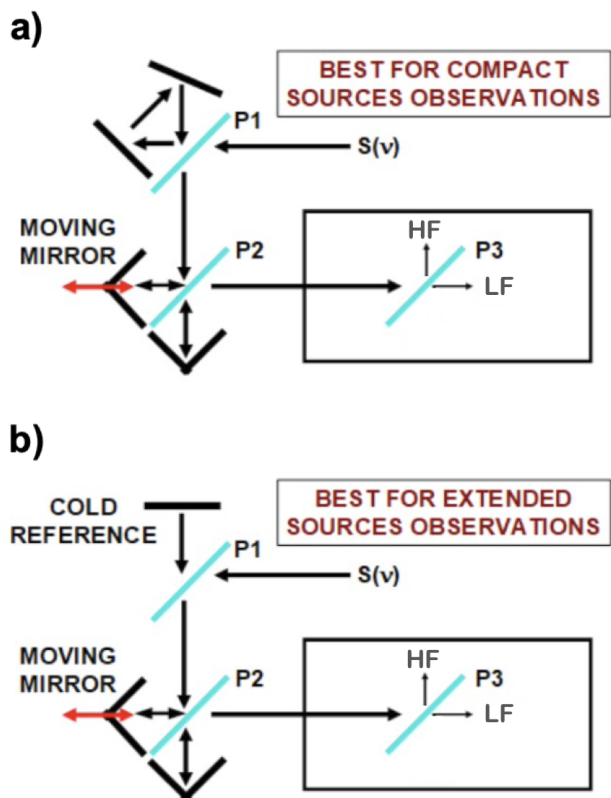


Fig. 1. Schematic view of the CONCERTO spectrometer. The incoming beam, represented by its spectral distribution S_ν , is directed through the MPI. Two options are implemented for the reference input: (a) a defocused image of the $\sim 18.6'$ instantaneous field of view (REFSKY), and (b) a stabilised cold blackbody source (REFBB). Polariser P1 and P2 are located at ambient pressure, while polariser P3 is housed in a cryostat together with the LF and HF detector arrays. P1 provides the polarised input to the MPI, P2 acts as the beam splitter defining the two interferometric arms, and P3 defines the two complementary outputs of the interferometer, which are directed to the two focal-plane arrays. The transmission output corresponds to the low-frequency (LF; 130–270 GHz) band, and the reflection output to the high-frequency (HF; 195–310 GHz) band.

makes them particularly well suited to the rapid sampling required to mitigate atmospheric instabilities and fast-varying interferograms (Catalano et al. 2020). The main source of systematic error may instead arise from the measurement of these resonance-frequency shifts, particularly when rapid variations in the background radiation move the detector resonance far from the fixed readout tone frequency.

Each frequency band is equipped with 2152 LEKIDs (Doyle et al. 2010). The detectors are coupled to planar antennas and are read out using frequency-division multiplexing, which allows 400 resonators to be monitored simultaneously over a single transmission line (Bourrion et al. 2022).

The practical implementation for one KID is illustrated in Fig. 2, which shows two representative interferometric blocks from COSMOS-field observations. Each block corresponds to a full cycle of rooftop-mirror movement, defining the OPD and setting the effective spectral resolution. This block-level organisation ensures that raw measurements can be efficiently transformed into calibrated interferograms and astrophysical spectra. A more detailed description of the acquisition chain, including mirror motion, sampling strategy, and KID readout, is presented

in Bounmy et al. (2022), Bourrion et al. (2022), and Désert et al. (2025).

3. Observations

We used a subset of COSMOS field observations obtained as part of the CONCERTO [CII] Line Intensity Mapping (LIM) Large Programme. Between July 2021 and December 2022, the project accumulated 793 hours on the field, combining rectangular and spiral on-the-fly (OTF) raster scans for a total of 1522 individual scans. These observations were acquired with REFBB as the reference source and span a wide range of atmospheric conditions (PWV = 0.3–3 mm) and source elevations (24° – 65°).

Each rectangular or spiral OTF scan corresponds to the mapping of a predefined RA/Dec region of the COSMOS field, with a typical scan duration of 20–25 minutes. During an individual scan, the elevation changes by approximately 1 – 8° , with the smallest variation occurring near transit and the largest variation at low elevations. Over the course of an observing session, the field is tracked from low elevation through transit, reaching a maximum elevation of about 65° .

For the present analysis, we exclusively used data extracted from individual scans, selecting as many contiguous subsets of 50 interferogram blocks (slices) as possible within a given scan. This approach limits the elevation range sampled within each subset, which is well suited to the forward-modelling and calibration analyses presented in this work, while maintaining computational efficiency. The LEKIDs were operated with fixed tuning parameters during each scan and were not re-tuned in response to elevation-dependent background variations within a scan (Bounmy et al. 2022). However, the detectors were re-tuned between scans to maintain optimal operating conditions.

4. Data reduction

The spectroscopic data reduction pipeline with REFSKY reference was partially described in Désert et al. (2025), and a complete description of the two reduction pipelines will be presented in Beelen et al. (in prep.). We distinguish between the time-ordered data (TOD), corresponding to the raw detector readout as a function of time, and the interferogram timelines, which are obtained after basic data reduction and scan reconstruction by mapping the TOD onto the optical path difference. The interferogram timelines therefore represent the reduced data products used as input to the forward modelling, rather than the original detector time streams. We summarise here the only two steps of the data reduction process that are relevant for the analysis presented in this work:

- (I,Q) to Hz: The raw time-ordered data (TOD) are recorded as in-phase (I) and quadrature (Q) components of the complex KID readout signal (not to be confused with Stokes parameters), corresponding to the mixing between the excitation tone and the detector output. The data are organised into blocks of 2048 samples per detector, sampled at 3814.7 Hz ($500 \text{ MHz}/2^{17}$, where 500 MHz is the original clock frequency). The conversion to a resonance frequency shift Δf in Hz is performed independently for each block (Fig. 2) using the three-point modulation algorithm (Fasano et al. 2021; Bounmy et al. 2022), in which the excitation tone is rapidly modulated between two known calibration frequencies and a science frequency corresponding to the tuned resonance. This scheme reconstructs the resonator (I,Q) circle and converts the measured phase signal into a resonance-frequency

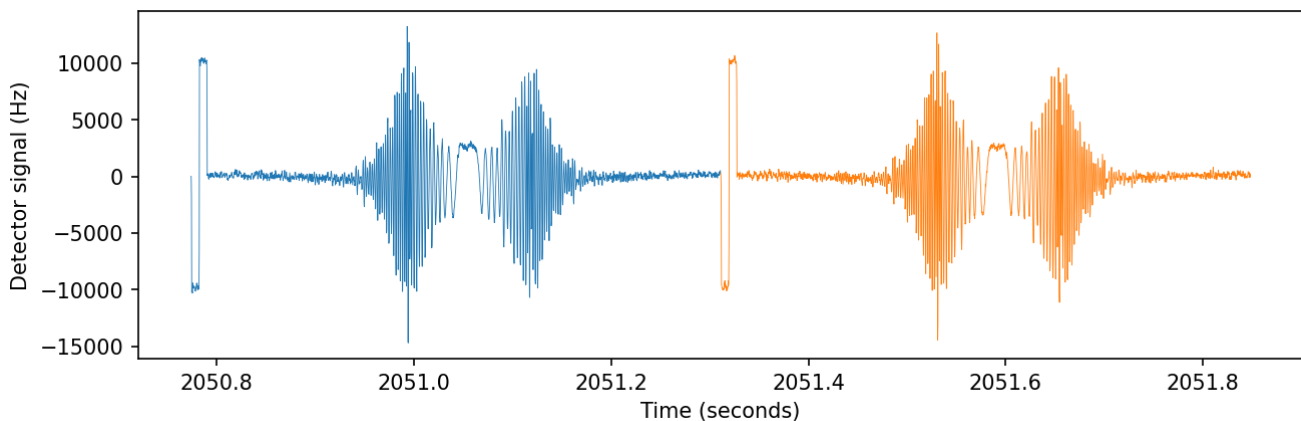


Fig. 2. Two representative interferometric blocks from real CONCERTO observations for one KID, with time on the x-axis and the detector signal (Hz) on the y-axis. Each block (shown in blue and orange) corresponds to a full rooftop-mirror round trip (forward and backward) scan, defining the optical path difference (OPD) and setting the effective spectral resolution. The first squared-shaped samples correspond to the modulation used for the three-point calibration (Bounmy et al. 2022). They are followed by the forward and then the backward interferogram.

shift, thereby reducing off-resonance systematic errors. In KID detectors, incident optical power modifies the kinetic inductance of the resonator, leading to a shift of its resonance frequency; this frequency shift therefore constitutes the detector response and explains why interferograms are expressed in units of Hz. The resulting Δf provides a calibrated measure of the optical load.

- KID selection: a careful identification and removal of non-optimal detectors before calibration and analysis is mandatory. As detailed in Hu et al. (2024), the selection process is based on a combination of stability, responsivity, and noise performance. Detectors exhibiting pathological behaviour, such as unstable resonance frequency, anomalous gain variations, or strong $1/f$ noise components, are flagged and excluded from subsequent processing. Additional rejection criteria are applied to detectors with persistent electronic cross-talk or with response patterns inconsistent with the optical beam.

5. Modelling the raw interferograms of CONCERTO

The modelling of CONCERTO’s instrumental response is naturally organised into two complementary steps. In spectral space, we describe the astrophysical and atmospheric signals together with the instrumental transmission, producing a compound spectrum. This spectrum is then transformed into Fourier space, yielding model interferograms that can be directly compared with the raw measurements.

The forward model is restricted to the dominant contributions that determine the large-scale structure of the interferograms. In the present implementation, we included atmospheric emission, the reference source, and a stray-light component, all filtered by the measured instrument bandpasses. Astrophysical sky emission is neglected because its contribution is small compared to the atmospheric and instrumental backgrounds for the calibration observations analysed here. We further assumed that the detector response is linear over the range of optical loading encountered in the data and that instrumental parameters such as the bandpass and stray-light contribution remain constant within a given scan. Under these assumptions, the model captures the leading-order behaviour of the interferograms while remaining computationally tractable for the large number of detectors and scans we considered.

In this way, the modelling follows the same flow as the data: the physical signals are naturally described in frequency space, while the instrument records them as interferograms.

5.1. Description in spectrum space

To interpret the measured interferograms, it is necessary to construct forward models of the signals entering the two beams of the spectrometer. On the one hand, the model accounts for the atmospheric emission, which varies with PWV and telescope elevation and must therefore be updated for each observation. The contributions of the reference source (REFBB) and stray light were kept fixed with respect to elevation and PWV in the present model.

The models were combined with the measured instrument bandpass to form a compound spectrum, which was then Fourier transformed into interferogram space. In this formulation, the bandpass is assumed to be stable during a scan, allowing the instrumental response to be represented by a fixed spectral weighting applied to the incoming radiation. This procedure ensures proper sampling of the interferograms, with the frequency range and spacing in spectrum space chosen to guarantee accuracy in Fourier space.

In the following subsections, we describe the three main ingredients of this modelling in more detail: the atmosphere, the reference source, and stray light.

5.1.1. Atmospheric contribution

The atmosphere is a major contributor to the CONCERTO signal, with its relative importance depending on frequency band and observing conditions. Away from strong atmospheric emission features, including the 183 GHz water vapour line, and at low PWV, the spectral atmospheric emission in the lower frequency range is typically lower than the contribution from the reference source. In contrast, in the upper frequency range, or at higher PWV, the atmospheric continuum becomes more dominant due to the increased radiative background.

To represent the atmospheric transmission and emission, the forward model makes use of the ATM code (Pardo et al. 2001, 2025), which combines spectroscopic line catalogues with a semi-empirical treatment of water vapour continuum absorption.

The model spectra exhibit the characteristic absorption features of water vapour and molecular oxygen, which are imprinted on the observed data and provide valuable anchors for validating the instrument’s frequency scale. In addition, the broadband level of atmospheric emission sets a significant fraction of the optical loading on the detectors, directly impacting sensitivity.

In order to model the atmosphere accurately while keeping the processing time manageable, we employed a pre-computed lookup table. For each observation, the atmospheric spectrum was retrieved from this table based on the PWV and telescope azimuth and elevation measured at the time of the scan. This strategy captures the main variations in atmospheric emission without requiring a full ATM run for every scan, and dense spacing between grid points ensured smooth coverage across parameter space.

5.1.2. Reference source contribution

In the case of REFBB observations, the second input beam of the instrument is fed by a dedicated internal reference source that provides a stable broadband spectrum against which the astronomical signal is measured. Its contribution is assumed to be constant in time and independent of observing conditions. The REFBB configuration is realised by a cryogenically cooled copper plate maintained at ~ 20 K using a pulse-tube cooler. The optical path of the reference source includes additional elements internal to the REFBB assembly: a 20 mm thick polypropylene window and two 0.25 mm thick Zitex layers thermally anchored at 50 K and 10 K, respectively, which serve to suppress infrared radiation. These elements are specific to the reference-source optical chain and are distinct from the sky-facing entrance optics of the CONCERTO camera (Fasano et al. 2024).

When modelled with the Planck law, these components yield an effective optical load temperature that increases smoothly from 43 K to 51 K over the frequency range 110–350 GHz, as characterised in Fasano et al. (2024). Although this effective load is characterised over a broad frequency range (110–350 GHz), the band-limited reference contribution relevant for the LF and HF channels is obtained naturally in our forward model by weighting this spectrum with the measured instrument bandpasses.

5.1.3. Stray-light contribution

In addition to the atmosphere and reference source, a small fraction of the detected signal originates from stray light within the optical paths. This includes thermal emission from warm surfaces of the instrument and residual pickup from outside the nominal beams. It was modelled as a Cassegrain receiver cabin (C-cabin) ambient-temperature blackbody, at 11°C (Fasano et al. 2024). Although subdominant, accounting for stray light ensures a more accurate representation of the interferogram baseline.

The net stray light, resulting from the difference between the two optical paths, was detected and quantified using sky-dip and COSMOS observations. The observed amplitudes agree with expectations from the instrument design and construction. In addition, a systematic geometric pattern of stray light across the focal plane is observed, with second-order variations correlated with telescope elevation. This behaviour is likely linked to slow deformations of the beam splitter projected onto the ground, which vary with elevation angle.

Following these results, we modelled the stray light as an empirically determined effective blackbody contribution origi-

nating from the C-cabin environment, corresponding to an optical load of ~ 28 K. This value reflects a net stray-light coupling factor of about 0.1 relative to the physical cabin temperature (284 K) and was derived from two approaches that agree within 1σ : fits to averaged COSMOS interferograms including a stray-light term, and an independent sky-dip analysis at zero optical path difference. We adopted this effective load as a first-order representation of the net stray-light contribution.

Including the contribution from REFBB (see Sect. 5.1.2), the total effective optical load increases to 71–78 K over the frequency range 110–350 GHz, which is subsequently band-limited by the instrument response for each channel. This reference load provides a stable and well-characterised baseline against which the atmospheric and astrophysical signals were measured.

5.1.4. Compound spectra

In addition to the individual signal components described above, the instrumental bandpass must be taken into account to combine them into a physically meaningful model spectrum. The bandpasses of the LF and HF arrays were used to combine the modelled atmospheric emission with the instrumental contributions (reference source and stray light) into forward-modelled interferograms, enabling a direct comparison with the measured data. We adopted these bandpasses from Hu et al. (2024), where they were measured by closing the APEX shutter and assuming blackbody illumination. This yields the relative spectral response appropriate for point sources or, equivalently, for Rayleigh–Jeans temperatures (see their Appendices B and C).

The total instrumental signal was modelled as the combination of the three main contributions (atmosphere, REFBB, and stray light). In the model, the atmospheric component was updated dynamically according to the contemporaneous PWV and elevation at the block level, in contrast to the reference source and stray-light contributions, which remained fixed. The sum of these three spectra was then weighted by the instrument bandpass (see Sect. 4) to form a compound spectrum, which was then Fourier-transformed to generate the interferogram. The approach allowed us to predict the expected shapes of interferograms under varying observing conditions.

For a given measured interferogram of a detector i , the reconstructed spectrum of the input signal can be written as

$$m_{i,\nu} = k_i \mathbb{B}_\nu \left[e^{-\tau_\nu AM} T_{i,\nu}^{cos} + (1 - e^{-\tau_\nu AM}) T_\nu^{atm} - T_\nu^{ref} - T_\nu^{str} \right], \quad (1)$$

where ν is the frequency, k_i is the detector-dependent calibration factor [Hz/K], \mathbb{B}_ν is the area-normalised bandpass [GHz $^{-1}$], $AM = 1/\sin(el)$ the airmass at elevation el , and τ_ν is the zenith opacity. The brightness temperatures T_ν^{atm} , T_ν^{ref} , and T_ν^{str} represent the atmosphere, the cold reference, and stray-light contributions, respectively, while $T_{i,\nu}^{cos}$ is the astrophysical signal.

The quantity $m_{i,\nu}$ represents a bandpass-weighted spectral contribution per unit frequency and is therefore expressed in units of Hz/GHz, where the numerator (Hz) reflects the change in the KIDs resonance frequency and the denominator (GHz) the spectral frequency.

Writing the measurement in temperature units ensures that the same bandpass function applies as for point sources (Hu et al. 2024).

Since $T_{i,\nu}^{cos}$ is typically extremely small compared to the other contributions, it can thus be neglected in the rest of this study,

$$m_{i,\nu} = k_i \mathbb{B}_\nu \left[\epsilon_\nu T_\nu^{atm} - T_\nu^{ref} - T_\nu^{str} \right], \quad (2)$$

where $\epsilon_v = 1 - e^{-\tau_v AM}$ is the atmospheric emissivity. The ATM model directly gives $\epsilon_v T_v^{atm}$ given the proper airmass and PWV content.

5.2. Description in interferogram space

While the astrophysical modelling is most naturally formulated in spectrum space, the instrument records data in interferogram space. Our forward data model must therefore transform the compound spectrum into the Fourier domain and evaluate it as a function of optical path difference (OPD), which is determined by the stroke of the moving mirror of the interferometer.

We denote the optical path difference by δ , which is set by the position of the moving mirror.

For each interferogram, the OPD was reconstructed from the internal laser metrology system. CONCERTO employed three metrology lasers to monitor different optical elements of the interferometer. To determine the optical path difference δ , we used the readout of the laser monitoring the moving rooftop mirror (*laser1*) together with that of a second laser (*laser3*) directed towards the P2 polariser membrane, which tracks residual vibrations after real-time correction. Earlier publications describe different subsets of this metrology system depending on the subsystem under study (e.g. Fasano et al. 2022). Their combined signal is defined as $laser = laser1 + laser3$, and the OPD is then computed as

$$\delta = 2 \times (laser - ZPD), \quad (3)$$

where the factor of two accounts for the double pass through the interferometer. The zero path difference (ZPD) corresponds to the position where the optical paths of the two arms of the MPI are equal. It is determined in Sect. 6.

5.3. From spectrum space to interferogram space

For comparison with the interferometric data, the compound spectrum described in Sect. 5.1.4 was transformed into the Fourier domain to generate the corresponding model interferograms.

In CONCERTO, this transformation is performed numerically using a discrete fast Fourier transform (FFT). Specifically, we applied a real-to-complex FFT to the model spectrum array, yielding the corresponding complex interferogram. We used the highest spectral resolution input spectrum model to define a spectral binning on which all input spectra and bandpass are linearly interpolated. This defines a maximum OPD that is much higher than the one available with the mirror course of CONCERTO. By padding the input spectra and bandpass, we also produced interferograms with a higher OPD sampling to resolve all physical features. This provided an oversampled model interferogram $I(\delta)$ as a function of optical path difference δ on a dense OPD grid. A linear interpolation was then constructed and evaluated at the measured OPD positions of each interferogram, thereby accounting for the slight irregular sampling of the mirror motion.

The interferograms derived from the compound spectra described above were fitted to the interferograms recorded by CONCERTO. The fitting procedure used as an initial guess a model value of the ZPD (derived in Sect. 6.1). The fit yielded refined estimates of the ZPD and the detector response k_i , which were stored in a database for subsequent use in the data reduction pipeline. The workflow is summarised in Fig. 3.

An accurate ZPD determination is essential, since even small offsets introduce phase errors in Fourier space, biasing the recovered spectra. For example, for a Gaussian line at 300 GHz, a ZPD error of 0.035 mm translates into a 10% decrease in the recovered line amplitude. The determination of k_i allowed us to derive a spectroscopic flatfield, assuming that the LEKIDs all see the same signal. Flatfielding is particularly important for on-the-fly (OTF) observations and multi-beam instruments, where the signal in each sky pixel is reconstructed from the combined contributions of many detectors.

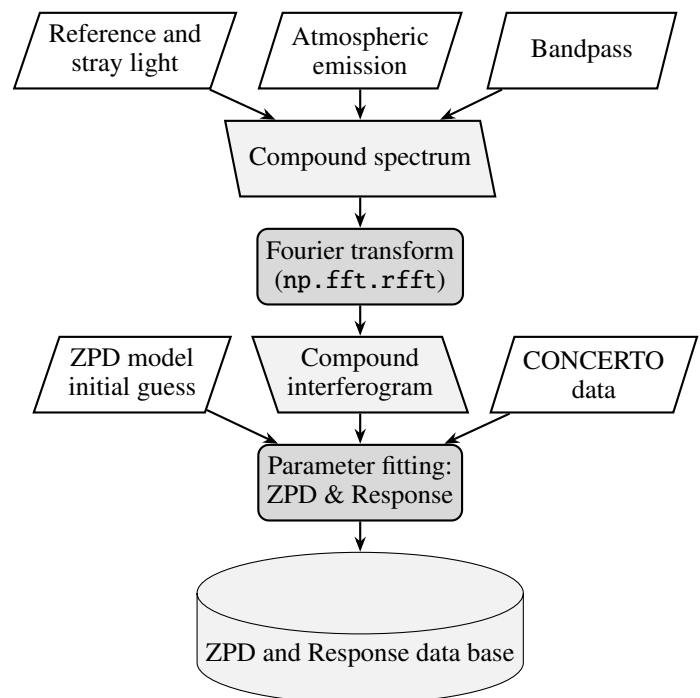


Fig. 3. Flow diagram of the forward model-fitting procedure. Atmospheric emission, reference source, and stray light are combined and filtered by the instrument bandpass to form the compound spectrum, which is Fourier transformed into the compound interferogram. Based on a model ZPD value as the initial guess (see Sect. 6.1), the interferogram is fitted to the data, yielding refined ZPD and response estimates that are stored in a database for later use.

With two frequency channels (LF and HF), about 1300 selected LEKIDs per array, and roughly 2830 science blocks per scan, each detector records about 5660 interferograms (forward and backward), corresponding to approximately 14.7 million science interferograms per scan across the full instrument. The fitting procedure treats each interferogram independently and in parallel, returning the two fitted parameters (ZPD and the detector response k_i).

We show in Fig. 4 the fitted interferogram models for the atmospheric contribution and the combined REFBB + stray light component (hereafter refstray) in the LF and HF channels for two clearly different cases of elevation and PWV. In the LF case, observed at low elevation and high PWV, the strong 183 GHz water-vapour line dominates the atmospheric signal, resulting in an interferogram where the atmospheric and refstray components contribute with comparable amplitudes. Their combination reproduces the measured data with remarkable accuracy, such that model and observation are nearly indistinguishable. In contrast, the HF case was obtained under drier conditions and at higher elevation, where the absence of strong atmospheric lines

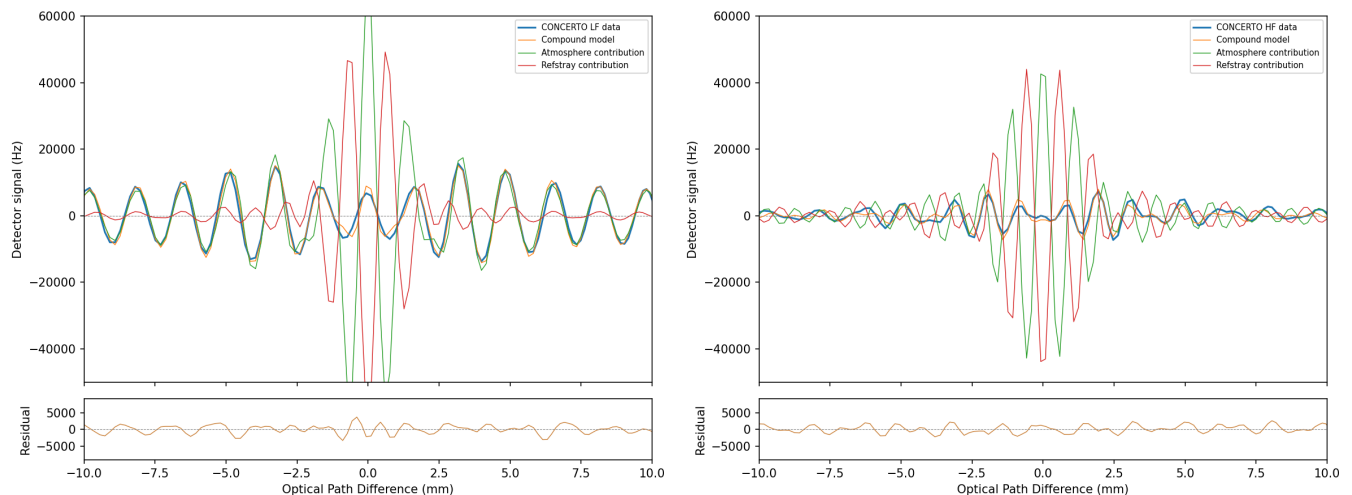


Fig. 4. Left panel: LF interferogram obtained at an elevation of 24° and PWV of 2.17 mm. In this band, the strong water-vapour line at 183 GHz produces a dominant atmospheric contribution (green), which is comparable in amplitude to the combined reference and stray-light emission (refstray; red). Their sum (orange) closely reproduces the observed data (blue), such that model and measurement nearly overlap. Right panel: HF interferogram at 41° elevation and PWV of 0.58 mm. The absence of strong atmospheric lines and the lower PWV here suppress atmospheric emission, leaving the refstray component as the main contributor. In both cases, the compound model tracks the data with high accuracy, with only small deviations visible away from the interferogram centre. Bottom panel: Residuals (data minus model).

left the refstray emission as the main contributor to the interferogram. The compound model closely tracks the data here as well.

6. Measuring the ZPD and the instrumental response from interferogram timelines

We present in this section the results obtained by comparing the forward model predictions with the measured interferograms and by optimising a limited set of instrumental calibration parameters, namely the ZPD (Sect. 6.1) and the relative detector response (Sect. 6.2). The underlying approach remains a forward modelling of the interferometric signal from physical inputs; the fitting procedure was used solely to determine these instrumental parameters and did not involve any inversion of the astrophysical spectra.

6.1. Zero path difference

For CONCERTO, the location of the ZPD varies across detectors and changes systematically with telescope elevation. These variations are likely related to small optical misalignments and elevation-dependent changes in the instrument geometry, although we did not attempt to model the underlying mechanical behaviour. To characterise this effect, we analysed a large number of COSMOS scans covering a wide range of PWVs and elevations.

We used the forward model to fit the ZPD for interferograms extracted from multiple COSMOS scans and grouped into slices of 50 interferogram blocks (see Sect. 3). From these fits, we derived an empirical description of the ZPD dependence on the two detector positions in the field of view and telescope elevation. This empirical model was then used to provide an initial estimate of the ZPD in the data reduction pipeline, where the ZPD was fitted for each block.

Figure 5 shows maps of the median ZPD for all valid detectors in the LF and HF arrays, derived from a COSMOS slice at 45° . The two arrays exhibit broadly similar, though not identical, spatial patterns. Forward and backward interferograms yield

nearly identical maps, but small systematic differences remain and must therefore be fitted separately.

In Fig. 6 we plot the median ZPD as a function of elevation for forward and backward interferograms. The fitted trends (third-order polynomials) capture the elevation dependence in both arrays. Over the elevation range sampled in this study (24° – 65°), the ZPD shifts reach peak-to-peak amplitudes of up to approximately 0.5 mm across the array. While we illustrate the array- and elevation-dependent variations separately (Figs. 5 and 6), in practice, they are fitted simultaneously over the full elevation range. This yields a three-dimensional empirical model of the predicted ZPD, combining detector position in the array with telescope elevation. The resulting model provides the initial guess for ZPD in the CONCERTO fitting procedure. The accuracy of this guess is critical: it must be better than 0.2 mm to prevent the fitting routine from locking onto a sidelobe instead of the true interferogram centre.

6.2. Diffuse emission spectroscopic flatfield

The relative response of each KID was determined from the same dataset used to establish the ZPD model. For each detector, we measured the median interferometric response and normalised it to the global array, deriving an interferogram-based flatfield. This flatfield is appropriate for diffuse emission in spectroscopic mode as it was derived mainly from atmospheric emission. It differs from the main-beam continuum flatfield presented in Hu et al. (2024), which is appropriate for point sources when CONCERTO operated in pure continuum mode.

After we accounted for the spectroscopic efficiency of the MPI, this diffuse spectroscopic flatfield showed strong similarities with the point-source continuum flatfield when the latter was converted into diffuse emission using the individual LEKID beams. This indicates that the spectroscopic efficiency is relatively uniform across the array.

In Fig. 7 we present the median normalised flatfield. Overall, the distribution of the flatfield shows a mild gradient perpendicular to the feed lines, with distinct zones reflecting the grouping of resonance frequencies of the LEKIDs along each line. These

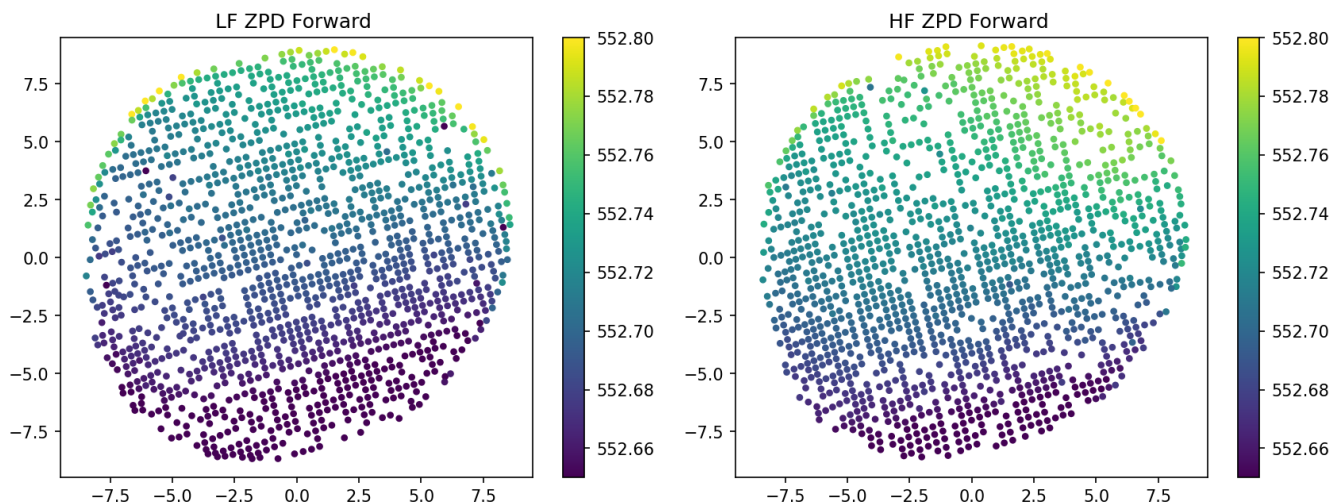


Fig. 5. Median ZPD values (in millimetres) derived for individual KIDs in the LF (left) and HF (right) arrays. Values are shown for forward interferograms; the backward solutions are nearly, though not exactly, identical and therefore must be fitted separately. The LF and HF maps exhibit very similar spatial patterns, but differ in absolute ranges (indicated by the colour bars). The sequence of the six feed lines is visible in both arrays, delineated by the empty lines. For clarity, these spatial variations are shown independently of the elevation dependence, though in practice, both effects are fitted simultaneously.

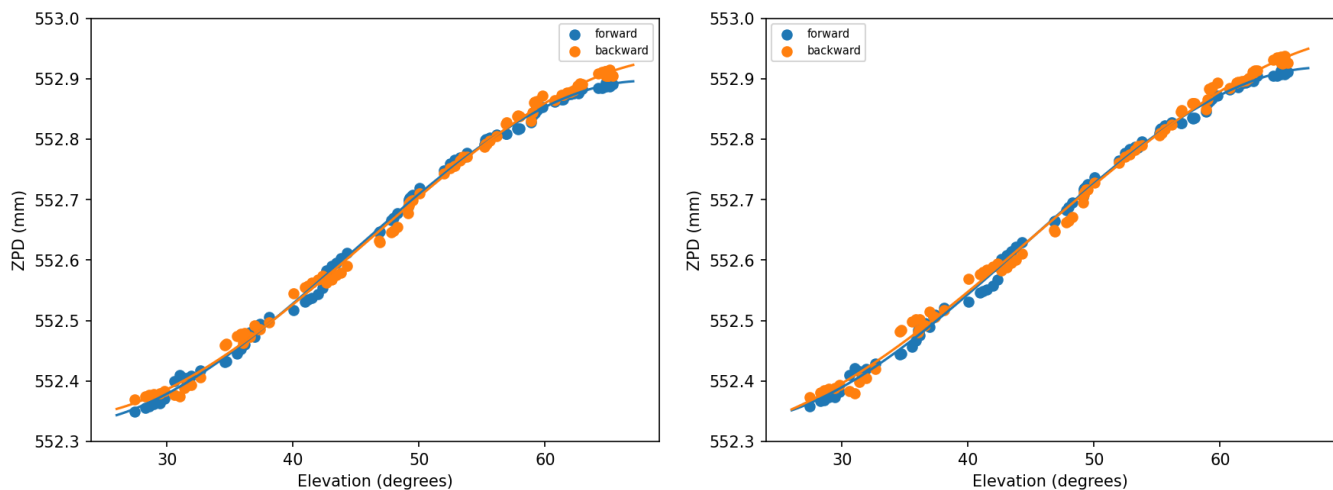


Fig. 6. Median ZPD (mm) as a function of elevation for forward (blue) and backward (orange) interferograms. LF is shown on the left and HF on the right, together with fitted curves describing the elevation trends. These trends are illustrated separately from the position-dependent variations across the arrays (Fig. 5), but in practice, both are modelled simultaneously to construct a three-dimensional empirical ZPD model.

groups correspond to electronic sub-bands, which are amplified with different gains to compensate for the intrinsic increase in readout noise at higher-resonance frequencies.

The derived flatfield is remarkably stable. Within a given observing run, flatfields obtained from different elevation slices are nearly identical, with only very small dispersions. The comparison of flatfields across different elevations and atmospheric conditions yields a median absolute deviation of 2-3% for the LF and HF arrays. This level of variation is small compared to the overall detector-to-detector response differences and indicates that the relative pattern of detector responses is highly preserved. These variations represent a minor contribution to the systematic uncertainty budget for line-intensity mapping with CONCERTO.

We stress that these values quantify relative variations in the flatfield pattern between observing conditions and no absolute calibration uncertainties. The high correlation coefficients indicate that the spatial response pattern is largely preserved.

These residual variations are small compared to the dominant atmospheric and foreground contributions in line-intensity mapping and are further mitigated by combining many detectors and scans in the map-making process. Day-to-day comparisons further confirm this stability, with rms differences below 0.05 and correlation coefficients above 0.96.

After the initial detector selection (see Sect. 4), about 1300 LEKIDs were retained for further analysis. We then calculated the flatfield and applied an additional validity criterion to ensure robust calibration: for each detector, the rms difference relative to reference flatfields had to remain below 0.07. This second cut excluded a further 40–50 LEKIDs that showed inconsistent or unstable responses across slices. For the detectors that passed both stages of selection, the flatfield values clustered tightly around unity, with ranges of 0.3–1.6 (standard deviation 0.17) for LF and 0.4–1.6 (standard deviation 0.21) for HF. These distributions reflect the intrinsic spread of detector responses while confirming the overall stability of the calibration. Some of the

detectors excluded in the second stage are shown in Fig. 7, which illustrates the flatfield distribution before applying this final cut.

7. Measuring the absolute brightness calibration factors from spectral cubes

The absolute brightness calibration factor is essential to translate interferometric timelines into astrophysical observables. Standard approaches rely on dedicated calibration procedures, such as planet observations, sky dips, or shutter measurements. These approaches, however, require external information (e.g. a model for the planet spectrum) or additional observing time and do not always capture the conditions of the science observations themselves (e.g. when using the shutter).

We introduce here a new method for recovering the absolute calibration factor directly from science data using the differential dependence of the measured spectra on elevation. In practice, the required airmass range is provided naturally by standard science observations, as the COSMOS field is tracked over several hours from low elevation through transit and back down, without the need for dedicated sky-dip measurements. Applied to fields without strong line emission, such as COSMOS, this approach effectively transforms regular science scans into calibration datasets. Beyond their immediate application to CONCERTO, it is broadly applicable to any instrument that combines wide-field spectroscopy with variable atmospheric transmission.

To make this explicit, when all LEKIDs were combined using the spectroscopic flatfield derived earlier and after we removed the contributions from atmospheric emission, the reference source, and stray light, the measurement (Eq. 1) can be rewritten as

$$m'_v = c'_v e^{-\tau_v AM} T_{i,v}^{cos}, \quad (4)$$

where $c'_v = k \mathbb{B}_v$ is the effective calibration factor directly applicable to the data, incorporating the bandpass \mathbb{B}_v and the absolute calibration factor k . The goal of this section is to show how c'_v can be derived.

An important consequence is that the slope of the signal variation with atmospheric conditions directly traces the product $k \mathbb{B}_v$. Therefore, the effective calibration spectrum (and thus, the instrumental bandpass shape up to an overall normalisation) can be determined directly from science observations. This behaviour is demonstrated explicitly using synthetic spectra in Appendix A.

7.1. The airmass method

The airmass method takes advantage of the dependence of atmospheric transmission on airmass to determine the absolute calibration factors and the instrumental bandpass. Differentiation of Eq. 2, where spectroscopic flatfield is applied, with respect to AM yields the slope \mathbb{S}_v ,

$$\frac{dm_v}{dAM} = \mathbb{S}_v = k \mathbb{B}_v \tau_v e^{-\tau_v AM} T_v^{atm}. \quad (5)$$

The slope \mathbb{S}_v can be measured directly at a given frequency from different airmasses. Physically, it quantifies how the atmospheric emission changes with airmass, thus providing a lever to extract the calibration factors.

With the slope definition (Eq. 5), the effective calibration factor can be related to \mathbb{S}_v as

$$c'_v = \frac{\mathbb{S}_v}{T_v^{atm} \tau_v e^{-\tau_v AM}}. \quad (6)$$

Thus, measuring the slope \mathbb{S}_v relative to the given T_v^{atm} allows us to derive the effective calibration factor.

7.2. The emissivity method

Alternatively, a slightly different method can be used that consists of deriving Eq. 2 with respect to ϵ_v . We obtain

$$\mathbb{S}_v^\epsilon = \frac{dm_v}{d\epsilon_v} = k \mathbb{B}_v T_v^{atm}, \quad (7)$$

and the effective calibration factor can then be written as

$$c'_v = \frac{\mathbb{S}_v^\epsilon}{T_v^{atm}}. \quad (8)$$

Furthermore, this method allows us to rewrite Eq. 2 as a linear relation,

$$m_v = \mathbb{S}_v^\epsilon \epsilon_v + m_v^0, \quad (9)$$

with

$$m_v^0 = -k \mathbb{B}_v (T_v^{ref} + T_v^{str}). \quad (10)$$

From this expression, it follows that

$$T_v^{tot} \equiv T_v^{ref} + T_v^{str} = -\frac{m_v^0}{\mathbb{S}_v^\epsilon} T_v^{atm}. \quad (11)$$

Compared to the airmass method, the emissivity method reparametrises the measurement in terms of atmospheric emissivity ϵ_v instead of airmass. This substitution often leads to a more direct linear relation between the signal and atmospheric conditions, simplifying the extraction of the calibration factors. While both approaches are formally consistent, the emissivity method can offer practical advantages when opacity and emissivity are more robustly constrained than the explicit airmass dependence.

The effective atmospheric brightness temperature T^{atm} and opacity τ_v were obtained from the ATM model using the PWV measured continuously by the APEX radiometer (Sarazin et al. 2013). During the scans used here, PWV typically varied by less than 0.2 mm, resulting in only small changes in the derived atmospheric spectra.

The uncertainties in T^{atm} mainly affect the overall absolute calibration scale because both calibration methods depend on $1/T^{atm}$. The dominant source of uncertainty in T^{atm} arises from the determination of the water-vapour column, while the intrinsic accuracy of the ATM model itself is at the level of $\sim 1\%$ (Pardo, priv. comm.).

For illustration, a conservative variation of ± 10 K around the typical value $T^{atm} \simeq 258$ K would translate into a change of $\sim 4\%$ in the derived calibration factors. A shift like this affects the airmass and emissivity methods in the same way, and it therefore does not affect their relative comparison (Fig. 9). The resulting absolute calibration uncertainty is consistent with the independent photometric calibration reported in Hu et al. (2024).

7.3. Practical implementation

For our analysis, we selected COSMOS scans away from transit (to maximise the range in airmass) and divided them into slices of 50 interferogram blocks (see Sect 3). Each slice was processed into an interferogram cube by combining all valid detectors using the spectroscopic diffuse flatfield and ZPD discussed earlier. The procedure is illustrated schematically in Fig. 8. Starting from the interferogram timeline data, we corrected for the

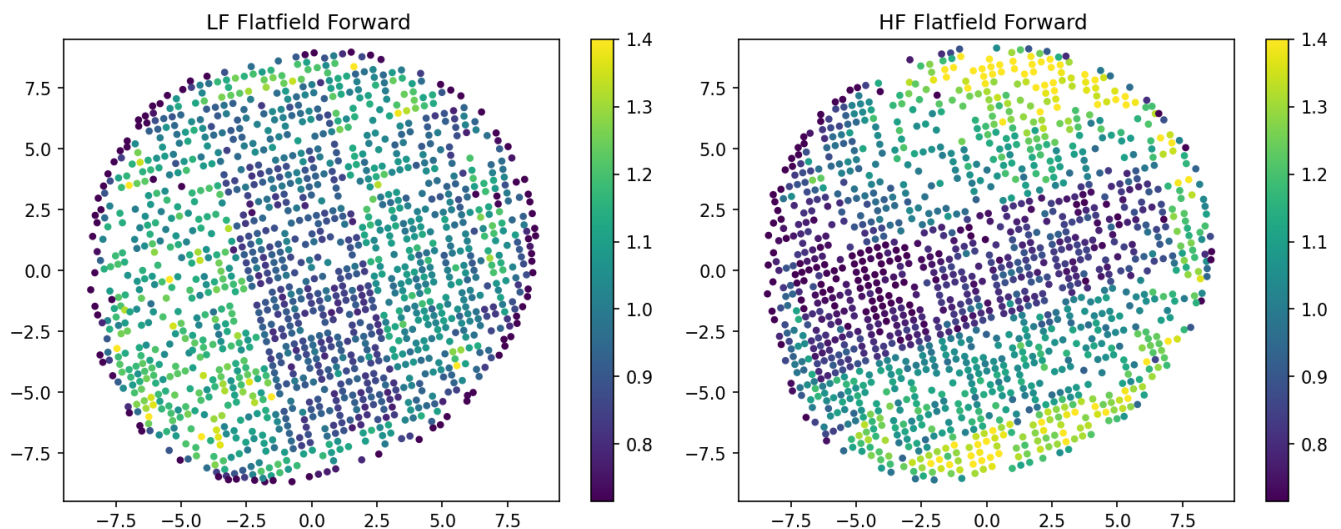


Fig. 7. Flatfields derived from the interferogram response to the forward model. The left (right) figure shows the LF (HF) array. We display the average response value for each LEKID, normalised to the global array median.

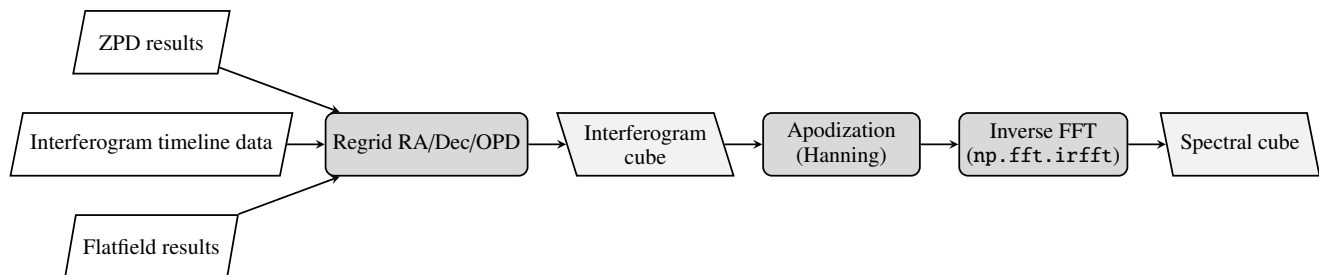


Fig. 8. Schematic illustration of the interferogram inversion pipeline. Interferograms are projected onto a RA/Dec/OPD grid (with input from ZPD and flatfield) to form an interferogram cube. The interferograms are apodised and inverted via inverse FFT along the OPD direction to be finally transformed into spectral cubes.

ZPD and applied detector flatfielding, both obtained using the forward model. The data were then rebinned in a common optical path difference (OPD) and projected onto a regular sky grid in right ascension and declination, producing interferogram cubes. These cubes were apodised along the OPD axis, typically with a Hanning window, and were subsequently inverted to spectrum space via an inverse Fourier transform. The result is a three-dimensional spectral cube, expressed in detector units as a function of sky position and electromagnetic frequency.

Each 25-minute scan was divided into approximately 60 slices of 50 interferogram blocks, corresponding to time intervals of about 25–30 s per slice. The slope determination therefore relies on a sequence of short quasi-instantaneous measurements rather than on a single long integration. During a typical scan, PWV variations are modest compared to the elevation-driven signal change; for example, in a representative COSMOS scan the median PWV is 2.96 mm with a standard deviation of 0.05 mm (minimum 2.87 mm, maximum 3.11 mm). As a result, the dominant variation of the signal arises from the systematic change in elevation, while residual atmospheric fluctuations mainly contribute to the scatter of the fit.

To validate the method, we first applied it to synthetic spectra replicating typical observing conditions (see Appendix A). The procedure successfully recovered instrument properties except near strong atmospheric lines. In these regions, the assumption of linear spectral variation with airmass is no longer valid, and

convolution of the strong lines with the instrumental sampling introduces spurious features that prevent reliable recovery.

7.4. Absolute spectral brightness calibration

The absolute calibration of CONCERTO spectroscopic data for point sources will be derived from Mars observations (Beelen et al. in prep.) by comparing dedicated calibration scans with the model of Lellouch & Amri (2008). In the previous subsections, we presented two alternative approaches for determining absolute calibration factors that are directly applicable to diffuse emission: the airmass method (Eq. 6), and the emissivity method (Eq. 8), which do not require prior knowledge of the precise instrument bandpasses.

In Fig. 9 we compare the effective calibration factors obtained with these two approaches for the LF and HF arrays. The figure demonstrates that both methods provide very consistent results, strengthening confidence in their use for extended sources.

Hu et al. (2024) derived the absolute photometric calibration factors by observing Uranus and comparing the measured flux to a well-established planetary model. This yielded calibration factors of 25.6 ± 0.9 Hz (Jy beam⁻¹)⁻¹ and 19.5 ± 0.6 Hz (Jy beam⁻¹)⁻¹ for the LF and HF channels, respectively (see their Fig. 12). We performed a rough consistency check between these calibration factors (point source and photometric mode) and those derived here (extended emission and spectroscopic mode).

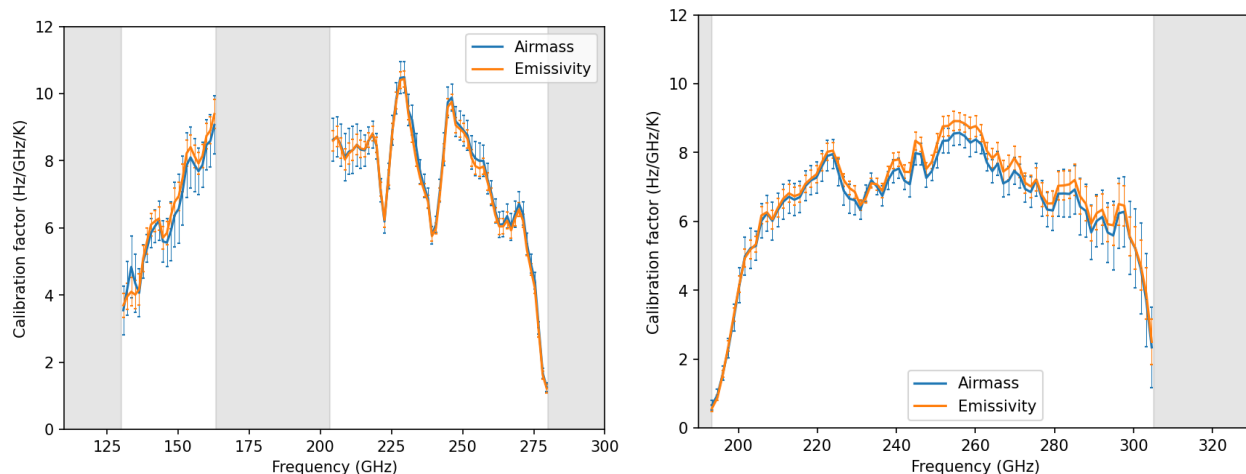


Fig. 9. Comparison of effective absolute spectral brightness calibration factors (k_{B_v}) derived using the airmass method (Eq. 6) and the emissivity method (Eq. 8) for the LF (left) and HF (right) arrays. Deviations near strong atmospheric lines are expected (masked by shaded areas), and these regions were excluded from the scientific analysis. The error bars indicate the 1σ uncertainties on the calibration factors obtained by propagating the uncertainties of the fitted slopes in the airmass and emissivity relations. The two methods yield very similar calibration spectra that agree within about 5% across the usable frequency range (excluding the shaded regions, where the fits are less reliable).

We first converted calibration factors from Hu et al. (2024) into Hz/GHz/K using the effective beam solid angles Ω_{eff} reported for 2022 in their Table 3, together with the conversion between MJy/sr and K provided in their Appendix C. The resulting values are 4.31 Hz/GHz/K and 4.41 Hz/GHz/K for LF and HF, respectively. Then these values had to be corrected for the interferometric efficiency, which quantifies the interferometric signal lost in the optics due to optical misalignment and chromatic effects in the optical components. As a first approximation, preliminary laboratory tests across the array indicate an interferometric efficiency of about 0.7. This gives calibration factors of ~ 6.2 Hz/GHz/K for the LF and HF, which compare well with our determinations (Fig. 9).

7.5. Independent estimate of the reference and stray-light temperatures

The emissivity method also provides an estimate of the combined temperature of the internal reference source and stray-light contribution (see Eq. 11). This constitutes an independent on-sky measurement that can be compared directly with the values adopted for the model (Sects 5.1.2 and 5.1.3), thereby serving as a verification of the accuracy of the model. These estimates rely on the intercept of the emissivity fit (Eq. 9), which corresponds to the combined reference-source and stray-light contribution. This offset is more sensitive to residual baseline fluctuations and modelling uncertainties than the slope, and its determination is therefore comparatively noisy. We derived averaged values (from 220 to 270 GHz) of 71.3 ± 3.4 K for LF and HF. This is slightly below but within the errors of the theoretical model, 74.2 ± 0.7 K, validating the modelling inputs and the emissivity method.

8. Conclusion

We have developed and applied an observation-driven forward-modelling framework to characterise and calibrate the CONCERTO spectrometer on APEX. By modelling the dominant instrumental and atmospheric contributions directly at the interferogram level, we established a coherent calibration chain linking

interferogram reconstruction to spectrum-space calibration. This approach enabled a robust determination of the zero path difference (ZPD), the relative detector responses, and the absolute spectral calibration factors directly from science observations.

Quantitatively, we found that the ZPD exhibits systematic elevation-dependent shifts of up to ~ 0.5 mm across the array, which are attributable to small optical misalignments and structural deformations. Correction of these on a per-interferogram basis reduced the residual errors to below 0.02 mm, avoiding amplitude losses in the reconstructed spectra. The flatfield derived from the response shows systematic variations with detector position, but is highly stable with time and observing conditions: comparisons across elevation and PWV regimes yielded rms differences of 0.04 (LF) and 0.042 (HF), mean absolute differences of 0.025 (LF) and 0.026 (HF), and correlation coefficients of 0.97 (LF) 0.98 (HF). These results demonstrate that the flatfield is essentially invariant over typical runs.

We further established two complementary absolute calibration routes that exploited atmospheric variation: the airmass method, and the emissivity method. Both methods yield consistent effective calibration factors that agree within 5% in the LF and HF bands. This validates the robustness of the forward-model approach and enables a direct conversion from detector units to astrophysical brightness units, without requiring detailed prior knowledge of the instrumental bandpasses. This is a real asset for a line-intensity mapping experiment.

Together, these results establish a coherent end-to-end calibration scheme for CONCERTO, linking interferogram correction (ZPD and flatfield) to the construction of calibrated spectral cubes with quantified systematics.

Future refinements will focus on (i) a formal uncertainty budget combining atmospheric and instrumental residuals, (ii) systematic comparison of the two calibration methods across the full range of atmospheric conditions sampled by the observations, (iii) improved modelling of elevation-dependent stray light, and (iv) a deeper characterisation of OPD deformations to better capture elevation-dependent effects.

Our method provides a solid foundation for the development and exploitation of future instruments of the same type, estab-

lishing a calibration framework that can inform the design and analysis of next-generation LEKID-based spectrometers.

Acknowledgements. We thank the anonymous referee for the careful reading and insightful comments, which have significantly improved the clarity and presentation of the article. We would also like to acknowledge the many technicians and engineers who contributed to the development of the CONCERTO experimental setup and its successful operation: Maurice Grollier, Olivier Exshaw, Anne Gerardin, Gilles Pont, Guillaume Donnier-Valentin, Philippe Jeantet, Mathilde Heigeas, Christophe Vescovi, Marc Marton, Christophe Hoarau, Jean-Paul Leggeri, Julien Marpaud, Samuel Roni, Damien Tourres, Sebastien Roudier, and Guillaume Bres. We acknowledge the crucial contributions of the whole Cryogenics and Electronics groups at Institut Néel and LPSC. We acknowledge the contributions of Hamdi Mani, Chris Groppi, and Philip Mauskopf (from the School of Earth and Space Exploration and the Department of Physics, Arizona State University) to cold electronics. The KID arrays of CONCERTO have been produced at the PTA Grenoble microfabrication facility. We warmly thank the support from the APEX staff for their support during observations and in CONCERTO pre-installations and design. The flexible pipes, in particular, have been routed under the competent coordination of Jorge Santana and Marcelo Navarro. We are grateful to our administrative staff in Grenoble and Marseille, in particular Patricia Poirier, Mathilde Berard, Lilia Todorov, and Valérie Favre, and the Protisvalor team. We acknowledge the crucial help of the Institut Néel and MCBT Heads (Etienne Bustarret, Klaus Hasselbach, Thierry Fournier, Laurence Magaud) during the COVID-19 restriction period. Based on observations with the APEX telescope under programme ID 108.21X2.001. APEX is a collaboration between the Max-Planck-Institut fuer Radioastronomie, the European Southern Observatory, and the Onsala Observatory. This work has been supported by the LabEx FOCUS ANR-11-LABX-0013, the European Research Council (ERC) under the European Union’s Horizon 2020 research and innovation programme (project CONCERTO, grant agreement No 788212), and the Excellence Initiative of Aix-Marseille University-A*Midex, a French “Investissements d’Avenir” programme. This work has also been supported by the GIS KIDS. MA is supported by FONDECYT grant number 1252054, and gratefully acknowledges support from ANID Basal Project FB210003 and ANID MILENIO NCN2024_112. This research made use of *Astropy* (<http://www.astropy.org>), a community-developed core Python package for Astronomy (*Astropy Collaboration et al. 2013, 2018*). We also use *Matplotlib* (<https://matplotlib.org>, (Hunter 2007)), *NumPy* (<https://numpy.org>, Harris et al. 2020) and *SciPy* (<http://www.scipy.org>, Virtanen et al. 2020).

References

- Adam, R., Adane, A., Ade, P. A. R., et al. 2018, *A&A*, 609, A115
Astropy Collaboration et al. 2013, A&A, 558, A33
Astropy Collaboration et al. 2018, AJ, 156, 123
 Bounmy, J., Hoarau, C., Macías-Pérez, J.-F., et al. 2022, *Journal of Instrumentation*, 17, P08037
 Bourrion, O., Hoarau, C., Bounmy, J., et al. 2022, *Journal of Instrumentation*, 17, P10047
 Catalano, A., Bideaud, A., Bourrion, O., et al. 2020, *A&A*, 641, A179
 Concerto Collaboration, Ade, P., & Aravena, M. o. 2020, *A&A*, 642, A60
 Désert, F.-X., Macías-Pérez, J. F., Beelen, A., et al. 2025, *A&A*, 701, A210
 Doyle, S., Mauskopf, P., Zhang, J., et al. 2010, in *Society of Photo-Optical Instrumentation Engineers (SPIE) Conference Series*, Vol. 7741, Millimeter, Submillimeter, and Far-Infrared Detectors and Instrumentation for Astronomy V, ed. W. S. Holland & J. Zmuidzinas, 77410M
 Fasano, A., Ade, P., Aravena, M., et al. 2024, in *Society of Photo-Optical Instrumentation Engineers (SPIE) Conference Series*, Vol. 13102, Millimeter, Submillimeter, and Far-Infrared Detectors and Instrumentation for Astronomy XII, ed. J. Zmuidzinas & J.-R. Gao, 131020O
 Fasano, A., Aguiar, M., Benoit, A., et al. 2020, *Journal of Low Temperature Physics*, 199, 529
 Fasano, A., Beelen, A., Benoit, A., et al. 2022, in *Society of Photo-Optical Instrumentation Engineers (SPIE) Conference Series*, Vol. 12190, Millimeter, Submillimeter, and Far-Infrared Detectors and Instrumentation for Astronomy XI, ed. J. Zmuidzinas & J.-R. Gao, 121900Q
 Fasano, A., Macías-Pérez, J. F., Benoit, et al. 2021, *A&A*, 656, A116
 Griffin, M. J., Abergel, A., Abreu, A., Ade, P. A. R., et al. 2010, *A&A*, 518, L3
 Güsten, R., Nyman, L. Å., Schilke, P., et al. 2006, *A&A*, 454, L13
 Harris, C. R., Millman, K. J., van der Walt, S. J., et al. 2020, *Nature*, 585, 357
 Hu, W., Beelen, A., Lagache, G., et al. 2024, *A&A*, 689, A20
 Hunter, J. D. 2007, *Computing in Science & Engineering*, 9, 90
 Kogut, A., Aghanim, N., Chluba, J., et al. 2025, *J. Cosmology Astropart. Phys.*, 2025, 020
 Lellouch, E. & Amri, H. 2008, *Mars Brightness Model*, <http://www.lesia.obspm.fr/perso/emmanuel-lellouch/mars/>, accessed: 2023-05-30

- Macías-Pérez, J. F., Fernández-Torreiro, M., Catalano, A., Fasano, A., et al. 2024, *PASP*, 136, 114505
 Maffei, B., Aghanim, N., Aumont, J., et al. 2024, in *Society of Photo-Optical Instrumentation Engineers (SPIE) Conference Series*, Vol. 13102, *Society of Photo-Optical Instrumentation Engineers (SPIE) Conference Series*, ed. J. Zmuidzinas & J.-R. Gao, 131020N
 Martin, D. H. & Pulett, E. 1970, *Infrared Physics*, 10, 105
 Masi, S., Battistelli, E., Brienza, D., et al. 2008, *Mem. Soc. Astron. Italiana*, 79, 887
 Mather, J. C., Fixsen, D. J., Shafer, R. A., Mosier, C., & Wilkinson, D. T. 1999, *ApJ*, 512, 511
 Monfardini, A. & Lagache, G. 2021, *Nature Astronomy*, 5, 970
 Monfardini, A., Swenson, L. J., Bideaud, A., et al. 2010, *A&A*, 521, A29
 Pardo, J. R., De Breuck, C., Muters, D., et al. 2025, *A&A*, 693, A148
 Pardo, J. R., Serabyn, E., & Cernicharo, J. 2001, *J. Quant. Spectr. Rad. Transf.*, 68, 419
 Sarazin, M., Kerber, F., & De Breuck, C. 2013, *The Messenger*, 152, 17
 Scoville, N., Aussel, H., Brusa, M., et al. 2007, *ApJS*, 172, 1
 Virtanen, P., Gommers, R., Oliphant, T. E., et al. 2020, *Nature Methods*, 17, 261

Appendix A: Validation on synthetic spectra at fixed atmospheric conditions

This appendix validates the absolute calibration methods introduced in the main text using synthetic data. While the results presented in the paper are derived entirely from real observations, the synthetic analysis provides a controlled test demonstrating that the airmass and emissivity methods correctly recover the calibration factors under idealised conditions.

A.1. Construction of synthetic spectra

Synthetic spectra were generated directly in frequency space for a fixed precipitable water vapour (PWV) of 2.9 mm, representative of typical COSMOS observing conditions. For each frequency bin, the atmospheric emission and opacity were computed using the ATM model (Pardo et al. 2001) over a range of telescope elevations matching those sampled during the science scans.

The synthetic measurements were constructed following Eq. 2 of the main text, including a representative instrumental bandpass and a fixed detector response factor. Only the atmospheric contribution was allowed to vary with elevation through its dependence on airmass, while the reference-source and stray-light contributions were kept constant.

Instrumental noise, bandpass uncertainties, stray-light variations, and elevation-dependent optical deformations were not included. The resulting dataset therefore represents an idealised case in which the assumptions underlying the airmass and emissivity calibration methods are exactly satisfied.

A.2. Application of the absolute calibration formalism

The synthetic spectra were analysed using the same procedures described in Sect. 7.2. For each frequency bin, the detector signal was fitted as a function of atmospheric emissivity,

$$\epsilon_\nu = 1 - e^{-\tau_\nu \text{AM}}, \quad (\text{A.1})$$

recovering the emissivity slope defined in Eq. 7. This slope directly traces the effective calibration spectrum $c'_\nu = k\mathbb{B}_\nu$, as defined in Sect. 7.

In the following subsections we first examine the linearity of the emissivity relation and then assess the recovery of the calibration factors.

A.3. Linearity with atmospheric emissivity

Before assessing the recovery of the calibration factors, we first verify the fundamental assumption underlying the emissivity method: that, at fixed PWV and over a limited elevation range, the detector signal varies linearly with atmospheric emissivity.

Figure A.1 shows synthetic spectra as a function of atmospheric emissivity for a fixed PWV of 2.9 mm and an elevation range of 26–33°. This relatively narrow interval corresponds to the typical elevation drift during a single 25-minute science scan. Each colour represents a distinct frequency channel within the LF (upper) and HF (lower) bands (blue = lowest frequency, red = highest frequency within each band), sampled at different elevations within this range. Identical frequency channels and colour coding are used consistently between the synthetic and real-data panels within each band.

In the synthetic case, the relation between detector signal and emissivity is strictly linear across the full elevation range.

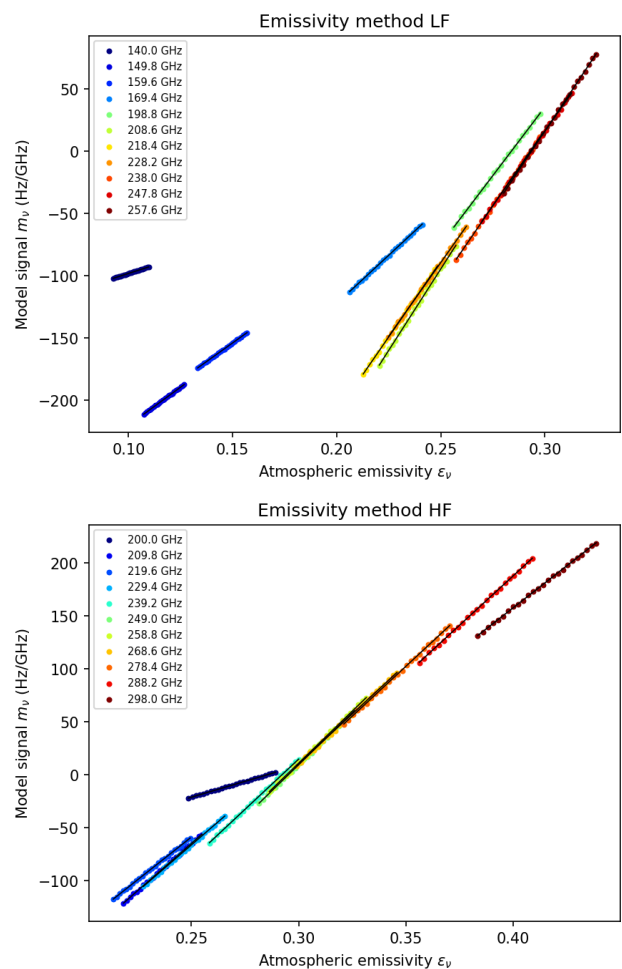


Fig. A.1. Synthetic spectra illustrating the linear dependence of the model signal on atmospheric emissivity under controlled conditions. The panels show the model signal as a function of atmospheric emissivity for representative frequency channels in the LF (upper) and HF (lower) bands for a fixed PWV of 2.9 mm and an elevation range of 26–33°. Each colour corresponds to a different frequency ν , and the solid black lines show the linear fits used to derive $dm_\nu/d\epsilon_\nu$ (Eq. 7). For visual comparison with the detector data, the synthetic spectra were multiplied by constant scaling factors to match the order of magnitude of the measured signal. Channels within ± 5 GHz of the 183 GHz water vapour line are omitted for clarity because their signals exceed the plotted dynamic range.

The fitted slopes reproduce the behaviour predicted by Eq. 7, confirming that under idealised conditions the emissivity-based formulation is mathematically exact.

For comparison, Fig. A.2 presents the same analysis applied to real CONCERTO observations at the same PWV and elevation range. While the data exhibit increased scatter due to instrumental noise and residual systematics, the linear trend with atmospheric emissivity remains clearly visible. Although the leverage in emissivity is modest (reflecting the limited elevation variation within a single scan), it is sufficient to constrain the slopes robustly.

These results validate the linear approximation underlying the emissivity method under realistic observing conditions and motivate the subsequent recovery of the effective calibration spectrum.

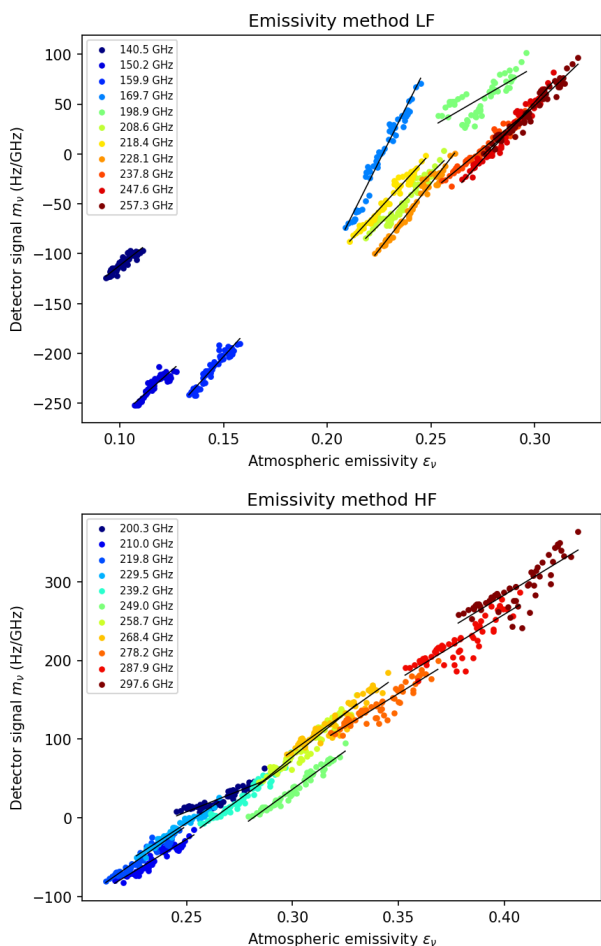


Fig. A.2. Measured detector signal as a function of atmospheric emissivity, for the same PWV (2.9 mm), elevation range (26–33°), and representative frequency channels shown in Fig. A.1. Colour coding follows the same convention as in the synthetic case (blue = lowest frequency, red = highest frequency within each band). Linear fits are overplotted for each frequency channel, from which $dm_\nu/d\epsilon_\nu$ (Eq. 7) is derived.

Compared to the synthetic case, the data exhibit increased scatter due to instrumental noise and residual systematics, while preserving the linear dependence on atmospheric emissivity.

A.4. Recovery of absolute calibration factors

Having established the linear dependence of the detector signal on atmospheric emissivity, we now assess whether the calibration factors can be quantitatively recovered from the synthetic data.

Because the synthetic spectra are generated from a known forward model, the input effective calibration spectrum $c'_\nu = k \mathbb{B}_\nu$ is known by construction. A representative instrumental bandpass and detector response factor were assumed to define this input spectrum.

Figure A.3 compares the calibration spectra recovered using the airmass and emissivity methods with the input calibration spectrum for the LF and HF bands. Across the usable frequency range, both methods recover the input calibration spectrum to within a few percent.

Noticeable deviations appear only in the vicinity of strong atmospheric absorption features, such as the 119 GHz oxygen line and the 183 and 325 GHz water vapour lines. In these regions the assumption of linear spectral variation with airmass or emissivity breaks down, as the sharp atmospheric line profiles

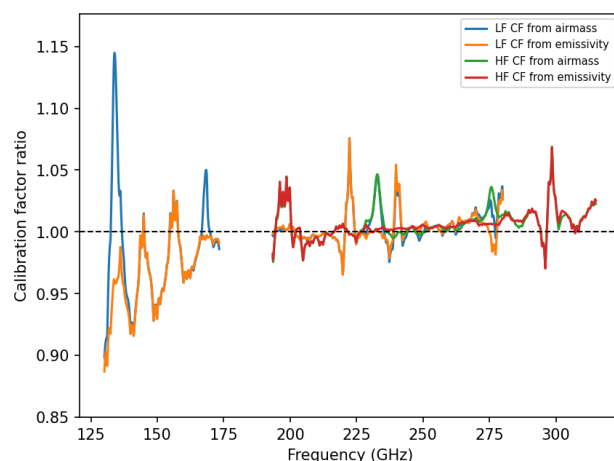


Fig. A.3. Recovery of the effective calibration spectrum $c'_\nu = k \mathbb{B}_\nu$ from synthetic data. The figure shows the ratio between the calibration factors recovered with the airmass and emissivity methods and the input calibration spectrum used to generate the synthetic spectra, for the LF and HF bands. Perfect recovery corresponds to a ratio of unity. Both methods reproduce the input calibration spectrum to within a few percent across the usable frequency range. Deviations occur only near strong atmospheric absorption features (e.g. the 183 GHz water vapour line and the 119 GHz oxygen line), where the assumption of linear spectral variation with airmass or emissivity breaks down due to the convolution of sharp atmospheric structures with the instrumental sampling. These frequency intervals are excluded from the scientific analysis in the main text.

are convolved with the instrumental spectral response. These frequency intervals are excluded from the scientific analysis in the main text.

We emphasise that, while the synthetic validation necessarily assumes a bandpass to construct the input spectra, the calibration factors derived from real data in Sect. 7 do not require prior knowledge of the bandpass shape. In the emissivity and airmass formulations, the recovered slopes directly trace the product $k \mathbb{B}_\nu$, allowing the effective calibration spectrum — and thus the bandpass shape up to an overall normalisation — to be determined directly from science observations.

A.5. Scope and limitations

This appendix demonstrates that the emissivity and airmass calibration methods are mathematically consistent and unbiased under controlled conditions where the assumptions of the forward model are exactly satisfied.

The synthetic validation isolates the calibration formalism by excluding instrumental noise, bandpass uncertainties, stray-light variations, and elevation-dependent optical deformations. Consequently, any deviations observed in real data must arise from additional physical or instrumental effects rather than from intrinsic limitations of the calibration method itself.

In practice, residual departures from ideal behaviour may result from atmospheric variability within a scan, imperfections in the optical path difference reconstruction, or elevation-dependent mechanical effects. These effects are addressed and quantified in the main body of the paper.

The present validation therefore confirms that, provided the linear emissivity regime holds, the calibration framework can recover the effective calibration spectrum directly from science observations without requiring prior knowledge of the bandpass shape.